

Electronic Supplementary Information (ESI)

Imine-linked donor-acceptor metal-organic frameworks for an efficient photocatalytic oxidative coupling reaction

Ri-Qin Xia, Tian-E Zhang, Zhen-Na Liu, Rong-Jia Wei*, Guo-Hong Ning*, Dan Li

College of Chemistry and Materials Science, Guangdong Provincial Key Laboratory of Functional Supramolecular Coordination Materials and Applications, Jinan University, Guangzhou 510632, People's Republic of China.

E-mail: rjwei@jnu.edu.cn, guohongning@jnu.edu.cn.

Contents

- 1.** General procedure
- 2.** Experimental section
- 3.** Fourier-transform infrared (FT-IR) spectra
- 4.** Solid-state ^{13}C CP/MAS NMR spectra
- 5.** Energy Dispersive X-ray Spectroscopy (EDS)
- 6.** X-ray photoelectron spectroscopy (XPS)
- 7.** Thermogravimetric analysis (TGA)
- 8.** Variable-Temperature PXRD
- 9.** Stability in various solvents
- 10.** Structural Simulation
- 11.** Photos for obtained samples
- 12.** Photocurrent response
- 13.** Mott-Schottky plot
- 14.** EPR experiment
- 15.** Evaluation of the $\text{O}_2^{\bullet-}$ generation efficiency
- 16.** Photocatalytic Application
- 17.** Computational Details
- 18.** Reference

1. General procedure

Powder X-ray diffraction (PXRD) data was collected at 40 kV, 30 mA using microcrystalline samples on a Rigaku Ultima IV diffractometer using Cu-K α radiation ($\lambda = 1.5418 \text{ \AA}$). The measurement parameters include a scan speed of 0.5 °/min, a step size of 0.02°, and a scan range of 2 θ from 1.5° to 30°. For temperature-dependent PXRD, the measurement parameters include a scan speed of 2 °C/min, a step size of 0.02°, and a scan range of 2 θ from 1.5° to 30°. Thermogravimetric analysis was performed on a Mettler-Toledo (TGA/DSC1) thermal analyzer. Measurement was made on approximately 5 mg of dried samples under a N₂ flow with a heating rate of 10 °C / min. The scanning electron microscopy (SEM) were obtained on Gemini300 Thermal Field Emission Scanning Electron Microscopy and Energy Dispersive X-ray Spectroscopy (EDS) images were obtained on a Helios Nanolab G3 CX microscope. Transmission electron microscopy (TEM) analysis was performed on FEI Talos F200X. Fourier transform infrared (FT-IR) spectrum was measured using a Nicolet Avatar 360 FT-IR spectrophotometer. X-ray photoelectron spectroscopy (XPS) experiments were performed by a Thermo ESCALAB 250XI system. GC-MS analysis was carried out on an Agilent 7890B GC analyzer. Liquid ¹H and ¹³C NMR spectra were recorded on a Bruker Biospin Avance (400 MHz) equipment using tetramethylsilane (TMS) as an internal standard. Solid-state NMR experiments were performed on a Bruker WB Avance II 400 MHz NMR spectrometer. The ¹³C CP/MAS NMR spectra were recorded with a 4-mm double-resonance MAS probe and with a sample spinning rate of 10.0 kHz; a contact time of 2 ms (ramp 100) and a pulse delay of 3 s was applied. Gas sorption analyses were conducted using an ASAP 2020 PLUS Analyzer (Micromeritics) with extra-high pure gases. Surface areas were calculated from the adsorption data using Brunauer-Emmett-Teller (BET) methods. The pore size distribution curves were obtained from the adsorption branches using density functional theory (DFT) method. Inductive Coupled Plasma (ICP) was measured by PerkinElmer OPTIMA 2000 ICP optical emission spectrometer.

2. Experimental section

All reagents were purchased from commercial suppliers and were used without further purification. 5''-(4'-Amino-[1,1'-biphenyl]-4-yl)-[1,1':4',1":3",1'''":4'',1'''-quinquephenyl]-4,4'''-diamine (**1**) and 3",4",5",6"-Tetrakis(4'-amino[1,1'-biphenyl]-4-yl)-[1,1':4',1":2",1'''":4'',1'''-Quinquephenyl]-4,4'''-diamine (**2**) were purchased from Jilin Chinese Academy of Science-Yanshen Technology Co., Ltd. **Cu₃L₃** was prepared according to the literature method.²

2.1 Preparation of JNM-18

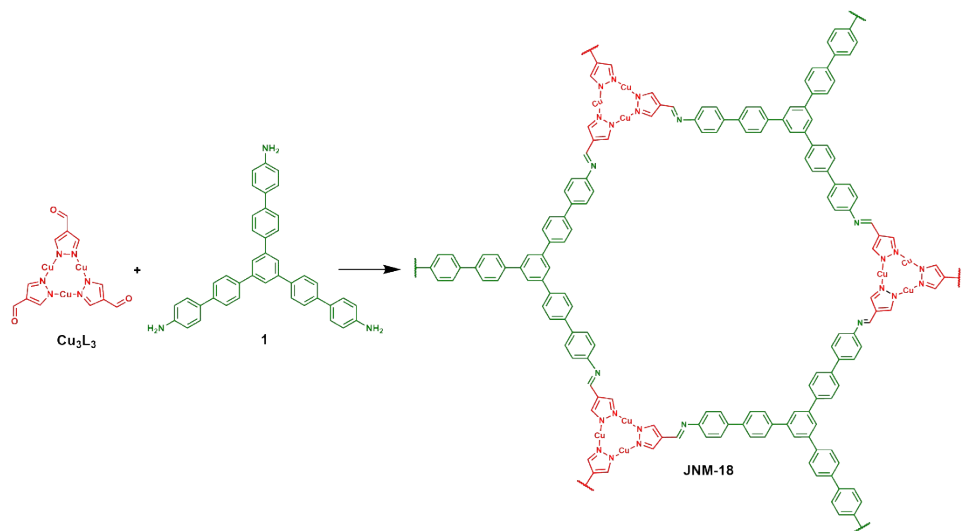


Fig. S1 Synthesis of **JNM-18**.

A 10 mL Schlenk tube was charged with **Cu₃L₃** (19.0 mg, 0.04 mmol), **1** (23.6 mg, 0.04 mmol), 1.0 mL of mesitylene, 1.0 mL of 1,4-dioxane and 0.2 mL of 6 M aqueous Acetic Acid (AcOH). The mixture was flash-frozen at 77 K in a liquid nitrogen bath and degassed with three freeze-pump-thaw cycles. Upon warming to room temperature, the mixture was heated at 120 °C for 72 h. Yellow powders were isolated by filtration, washed and solvent exchanged with DMF and EtOH. The resultants were dried under vacuum at 100 °C for 8 h. Yield: 37.8 mg (88.7%, based on Cu). Elemental analysis calcd for C₅₄H₃₆Cu₃N₉ (%): C 64.76, H 3.62, N 12.59; Found: C 61.71, H 3.70, N 9.05.

2.2 Preparation of JNM-19

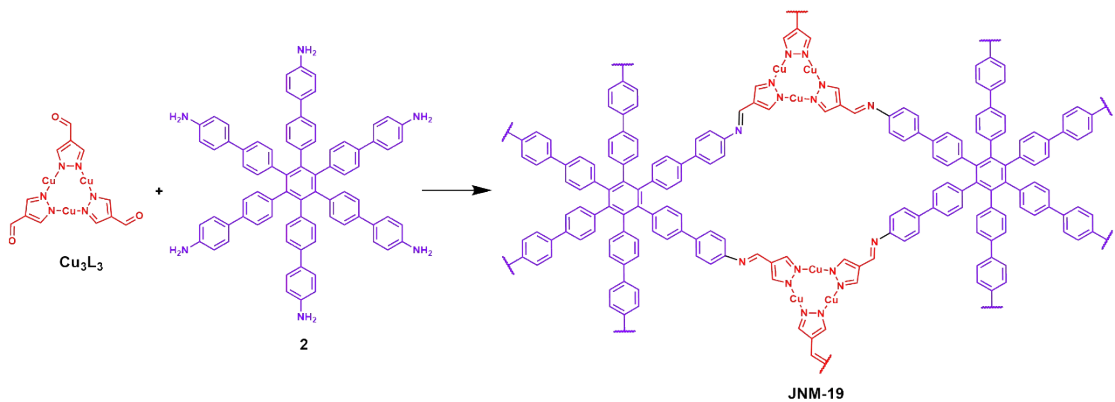


Fig. S2 Synthesis of **JNM-19**.

A 10 mL Schlenk tube was charged with **Cu₃L₃** (19.0 mg, 0.04 mmol), **2** (22.0 mg, 0.02 mmol), 1.0 mL of 1,2-dichlorobenzene, 1.0 mL of 1-Butanol and 0.2 mL of 6 M aqueous Trifluoroacetate (CF₃COOH). The mixture was flash-frozen at 77 K in a liquid nitrogen bath and degassed with three freeze-pump-thaw cycles. Upon warming to room temperature, the mixture was heated at 120 °C for 72 h. The brown-green powders were isolated by filtration, washed and solvent exchanged with EtOH and DMF. The resultants were dried under vacuum at 100 °C for 8 h. Yield: 37.0 mg (90.2%, based on Cu). Elemental analysis calcd for C₁₀₂H₆₆Cu₆N₁₈ (%): C 63.64, H 3.46, N 13.10; Found: C 59.79, H 4.05, N 9.20.

2.3 Optimization of synthesis of **JNM-18** and **JNM-19**

The selection of reaction solvent was found to be significant to the crystallinities of the products. Controlled experiments revealed the sample obtained in a 5: 5: 1 (v/v) reaction mixture of mesitylene, 1,4-dioxane, and 6 M aqueous acetic acid (AcOH) showed the best crystallinity for **JNM-18** (Fig. S3), while the optimized reaction solvent for **JNM-19** was the 5: 5: 1 (v/v) mixture of 1,2-dichlorobenzene, 1-butanol and 6 M aqueous trifluoroacetate (TFA) (Fig. S4).

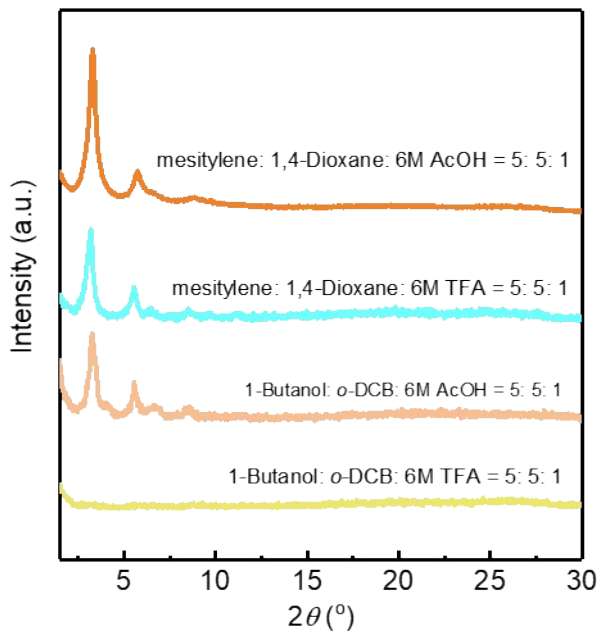


Fig. S3 Comparison of **JNM-18** synthesized in different solvents.

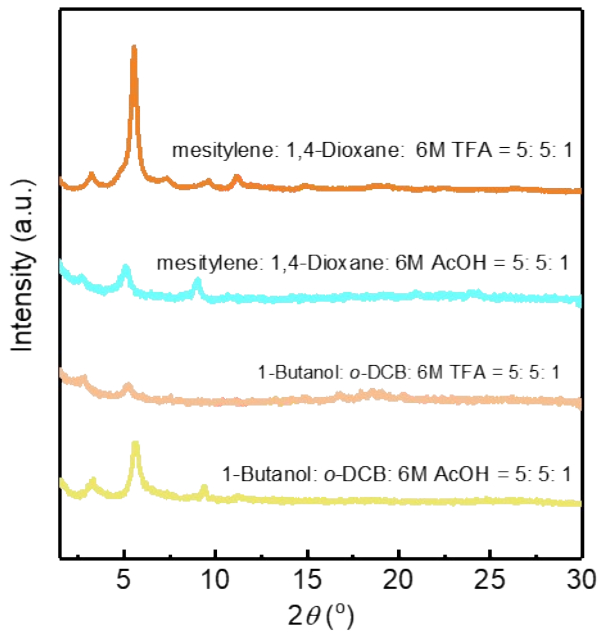


Fig. S4 Comparison of **JNM-19** synthesized in different solvents.

3. Fourier-transform infrared (FT-IR) spectra

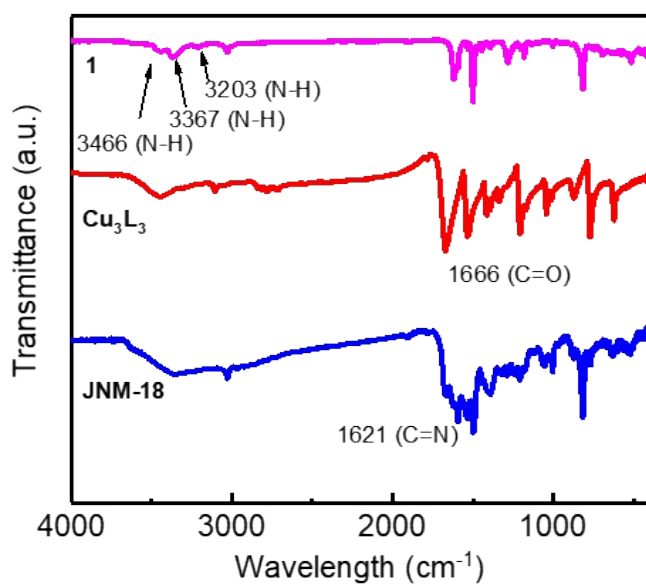


Fig. S5 FT-IR spectra of **1**, **Cu₃L₃**, **JNM-18**.

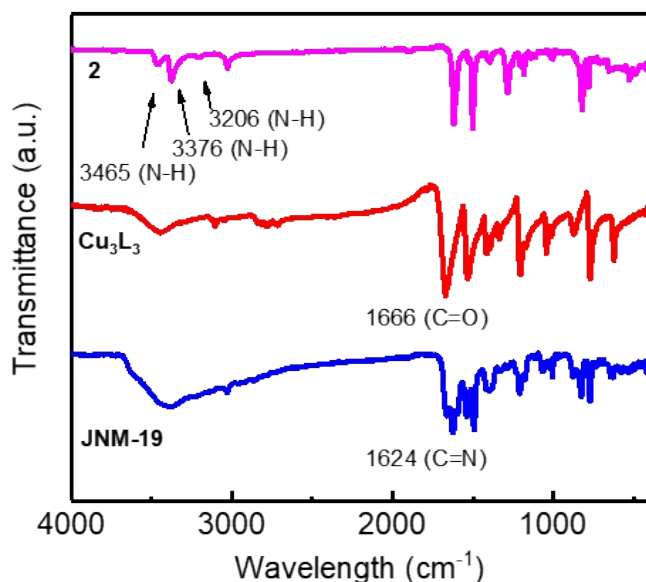


Fig. S6 FT-IR spectra of **2**, **Cu₃L₃**, **JNM-19**.

4. Solid-state ^{13}C CP/MAS NMR spectra

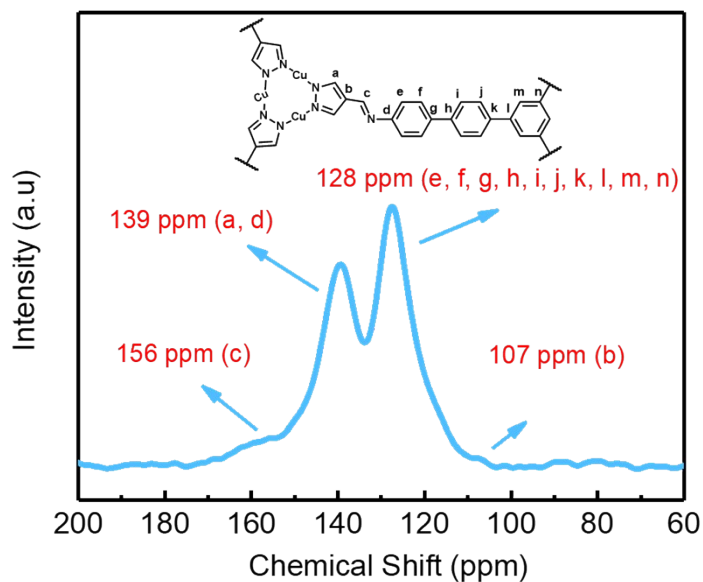


Fig. S7 Solid-state ^{13}C CP/MAS NMR spectra and peak assignments of **JNM-18**.

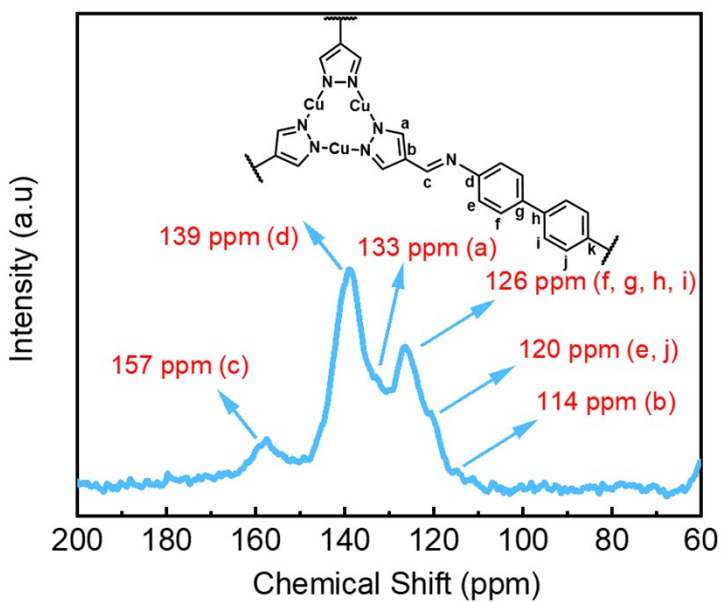


Fig. S8 Solid-state ^{13}C CP/MAS NMR spectra and peak assignments of **JNM-19**.

5. Energy Dispersive X-ray Spectroscopy (EDS)

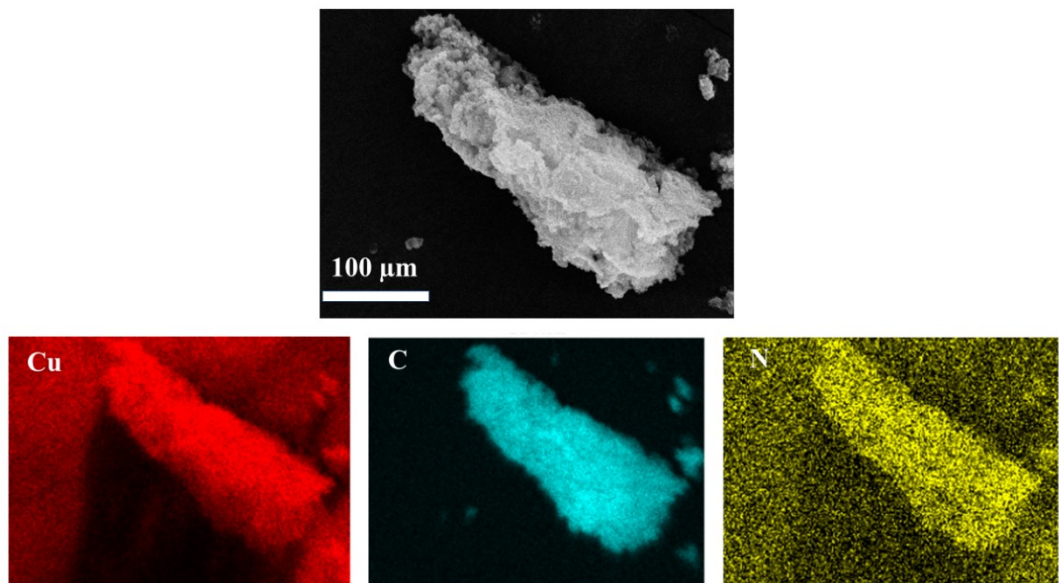


Fig. S9 EDS of JNM-18 showing the uniform distribution of element C, N and Cu.

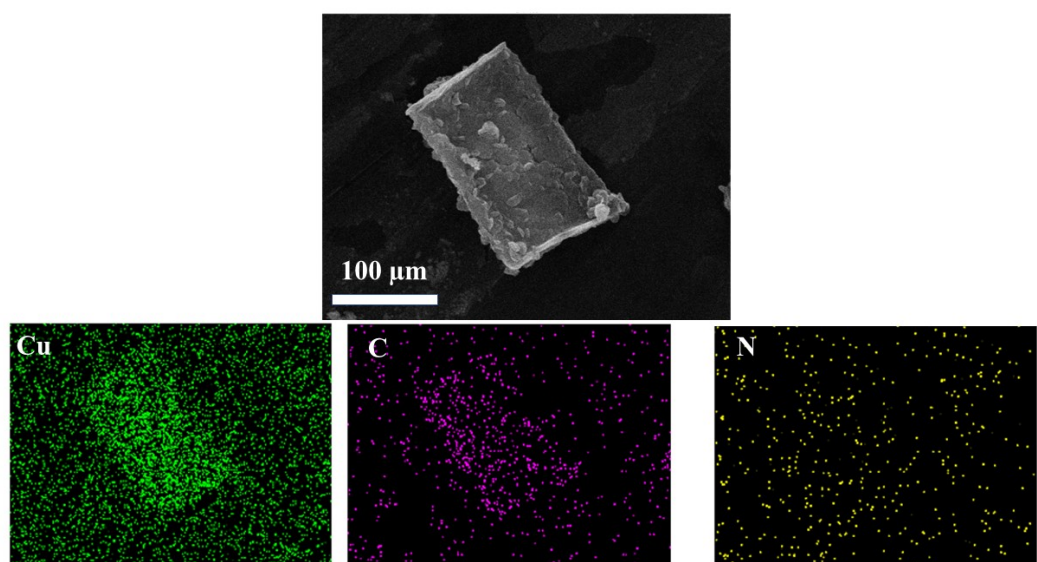


Fig. S10 EDS of JNM-18 showing the uniform distribution of element C, N and Cu.

6. X-ray photoelectron spectroscopy (XPS)

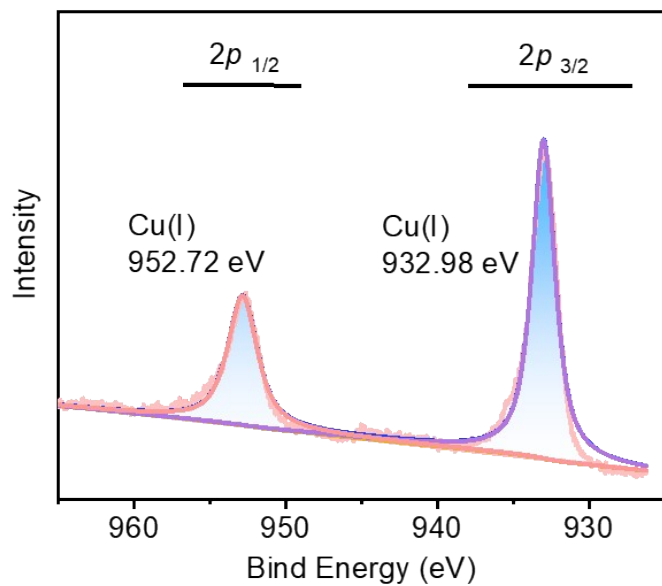


Fig. S11 XPS of JNM-18.

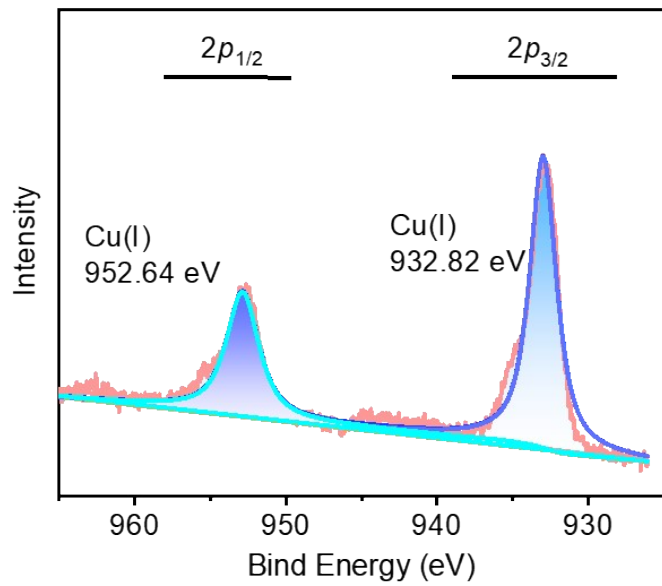


Fig. S12 XPS of JNM-19.

7. Thermogravimetric analysis (TGA)

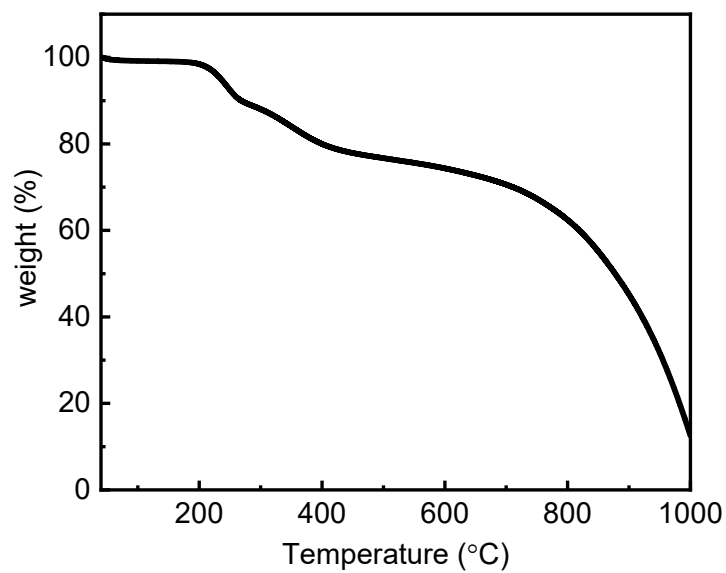


Fig. S13 TGA of **JNM-18** under N₂ atmosphere.

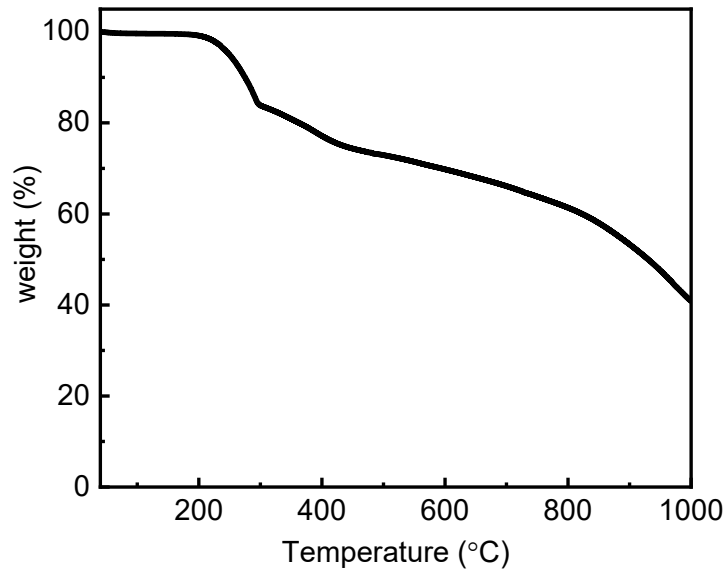


Fig. S14 TGA of **JNM-19** under N₂ atmosphere.

8. Variable-Temperature PXRD

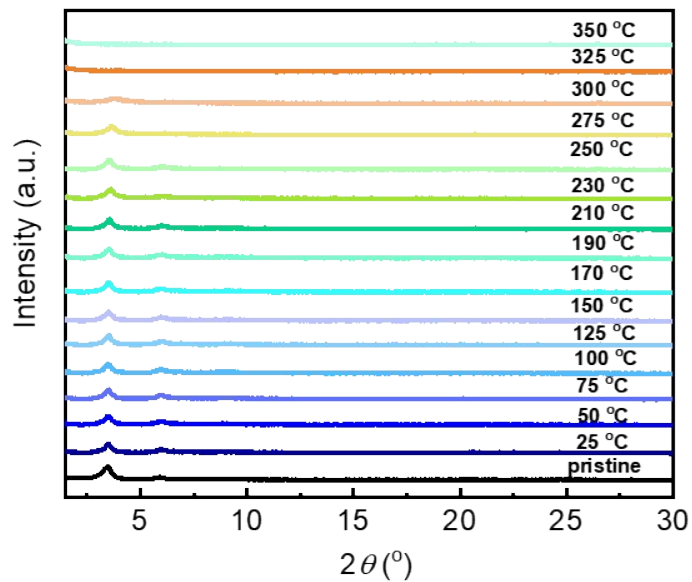


Fig. S15 *In-situ* variable-temperature PXRD patterns of **JNM-18**.

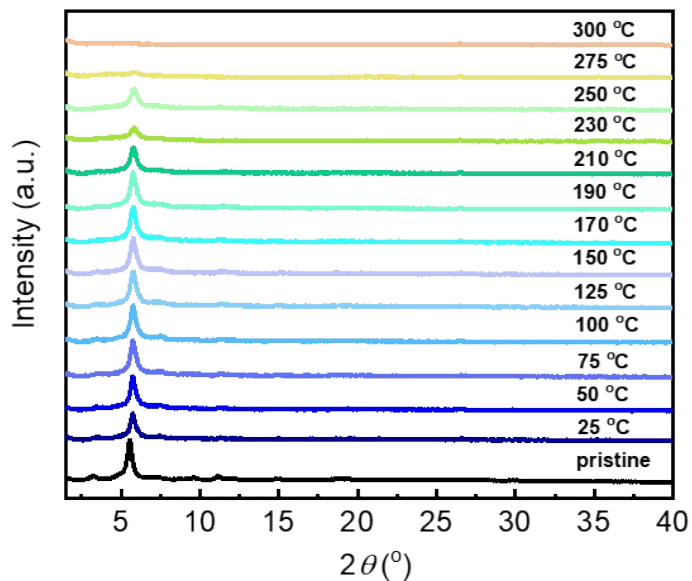


Fig. S16 *In-situ* variable-temperature PXRD patterns of **JNM-19**.

9. Stability in various solvents

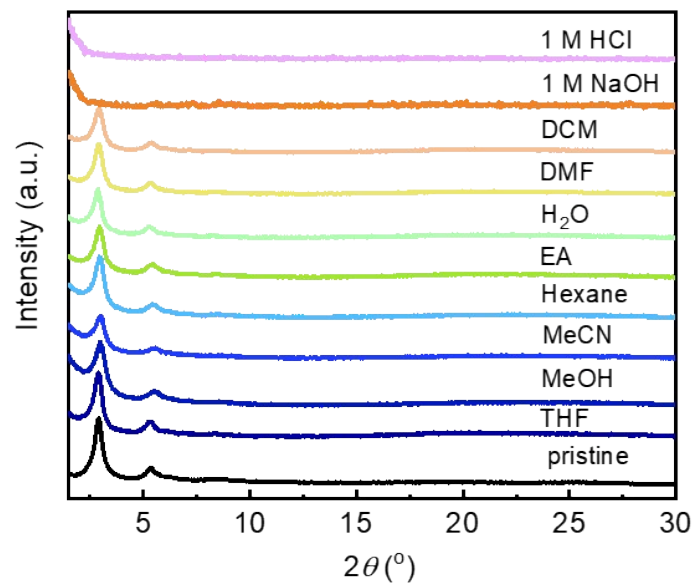


Fig. S17 PXRD patterns for samples of **JNM-18** after treatment with different solvents for 24 h.

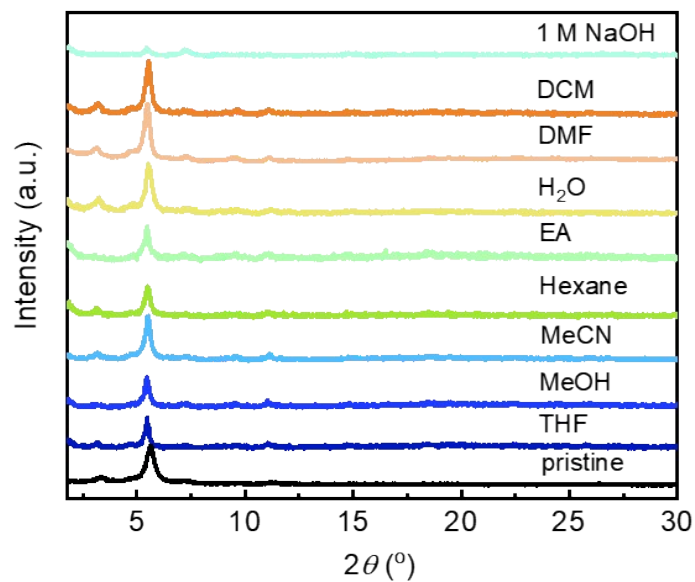


Fig. S18 PXRD patterns for samples of **JNM-19** after treatment with different solvents for 24 h.

10. Structural Simulation

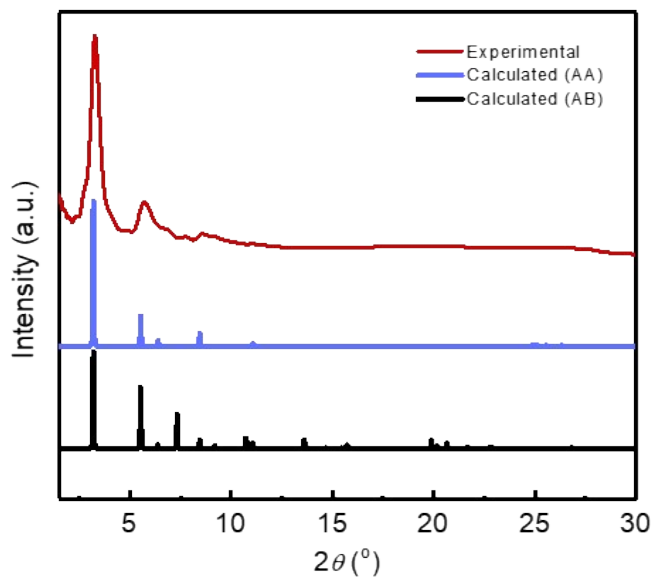


Fig. S19 Comparison of experimental and calculated PXRD patterns for **JNM-18**.

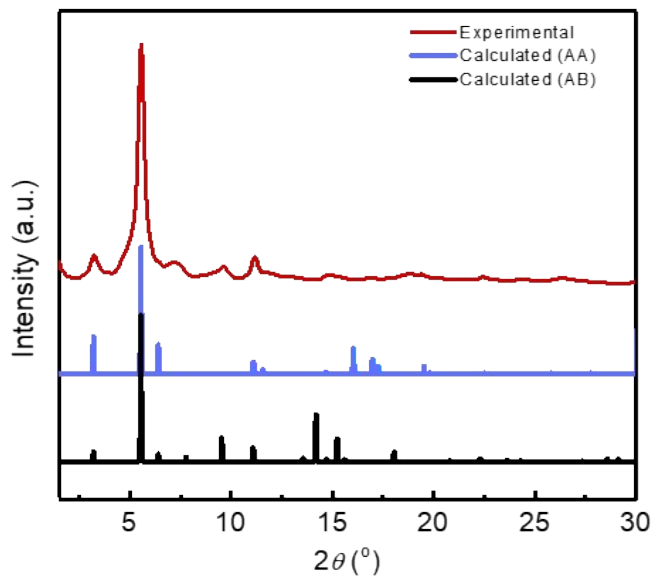


Fig. S20 Comparison of experimental and calculated PXRD patterns for **JNM-19**.

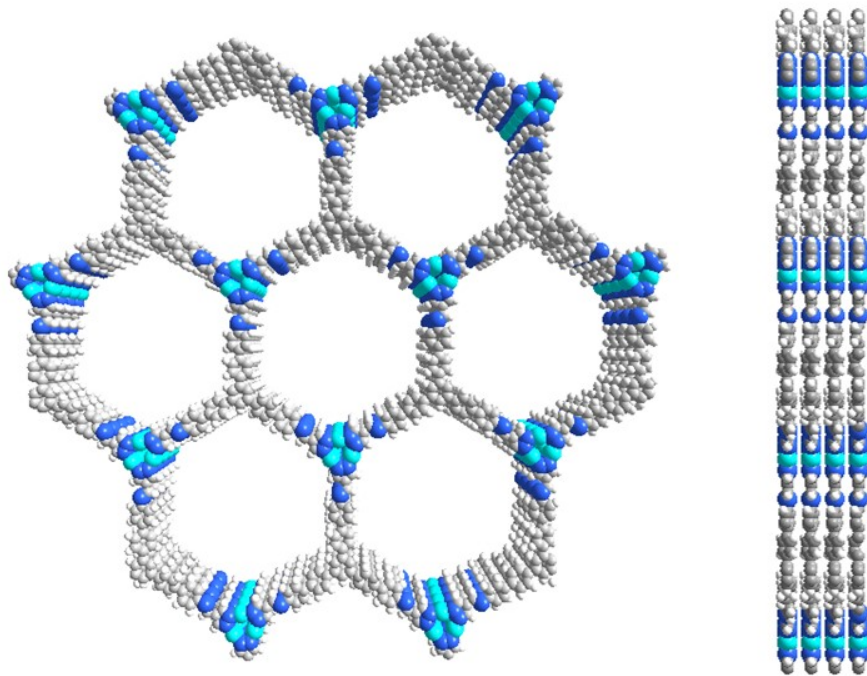


Fig. S21 Top (left) and side (right) views of **JNM-18** in AA stacking model.

Table S1. Atomic coordinates of the AA-stacking mode of **JNM-18**.

	Space group: <i>P</i> 3		
	<i>a</i> = <i>b</i> = 31.94 Å, and <i>c</i> = 3.57 Å	$\alpha = \beta = 90^\circ$, and $\gamma = 120^\circ$	
C1	0.30799	0.69177	0.02339
C2	0.35885	0.71795	0.02329
C3	0.07154	0.5351	0.01828
C4	0.04588	0.48557	-0.06844
C5	-0.00461	0.46029	-0.07091
C6	-0.03052	0.48383	0.01017
C7	-0.00497	0.53334	0.1017
C8	0.04555	0.55865	0.10432
N9	0.91758	0.45586	0.00474
C10	0.52729	0.41535	0.0053
C11	0.6107	0.4224	0.00256
N12	0.62644	0.39049	0.0012
N13	0.58905	0.34618	0.00089
C14	0.54796	0.34803	0.00189

C15	0.56056	0.3963	0.00297
Cu16	0.59718	0.28974	0.001
H17	0.06482	0.4665	-0.14036
H18	-0.02371	0.42219	-0.14032
H19	-0.02344	0.55261	0.17875
H20	0.06429	0.59651	0.18106
H21	0.63377	0.46127	0.0035
H22	0.51192	0.31688	0.00238
C23	0.38635	0.61415	1.02253
C24	0.3656	0.56702	0.87346
C25	0.39076	0.54171	0.87709
C26	0.43793	0.56312	1.02015
C27	0.45914	0.61021	1.16456
C28	0.43356	0.63511	1.17052
H29	0.4889	0.38993	0.00038
H30	0.33044	0.54977	0.74171
H31	0.37386	0.50589	0.75532
H32	0.49502	0.62727	1.28538
H33	0.45067	0.67022	1.30297
H34	0.28844	0.71113	0.02333

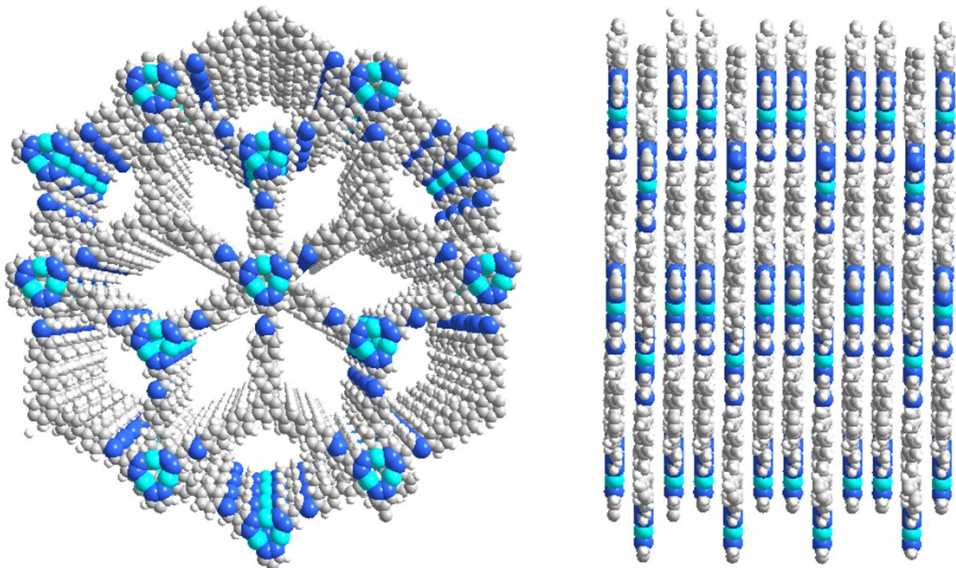


Fig. S22 Top (left) and side (right) views of **JNM-18** in AB stacking model.

Table S2. Atomic coordinates of the AB-stacking mode of **JNM-18**.

Space group: *P*3
 $a = b = 31.94 \text{ \AA}$, and $c = 13.38 \text{ \AA}$
 $\alpha = \beta = 90^\circ$, and $\gamma = 120$

	X	Y	Z
C1	0.30799	0.69177	0.16704
C2	0.35885	0.71795	0.16701
C3	0.07154	0.5351	0.16568
C4	0.04588	0.48557	0.14253
C5	0.99539	0.46029	0.14187
C6	0.96948	0.48383	0.16351
C7	0.99503	0.53334	0.18794
C8	0.04555	0.55865	0.18864
N9	0.91758	0.45586	0.16206
C10	0.52729	0.41535	0.16221
C11	0.6107	0.4224	0.16148
N12	0.62644	0.39049	0.16112
N13	0.58905	0.34618	0.16103
C14	0.54796	0.34803	0.1613
C15	0.56056	0.3963	0.16159
Cu16	0.59718	0.28974	0.16106
C17	0.38635	0.61415	0.16681
C18	0.3656	0.56702	0.12702
C19	0.39076	0.54171	0.12799
C20	0.43793	0.56312	0.16618
C21	0.45914	0.61021	0.20472

C22	0.43356	0.63511	0.20631
C23	0.64132	0.35844	0.50037
C24	0.69218	0.38462	0.50035
C25	0.40487	0.20177	0.4918
C26	0.37921	0.15224	0.47586
C27	0.32872	0.12696	0.4752
C28	0.30281	0.1505	0.49685
C29	0.32836	0.20001	0.52128
C30	0.37888	0.22532	0.52198
N31	0.25091	0.12253	0.4954
C32	0.86062	0.08202	0.49555
C33	0.94403	0.08907	0.49481
N34	0.95977	0.05716	0.49445
N35	0.92238	0.01285	0.49437
C36	0.88129	0.0147	0.49463
C37	0.89389	0.06297	0.49492
Cu38	0.93051	0.95641	0.4944
C39	0.71968	0.28082	0.50014
C40	0.69893	0.23369	0.46035
C41	0.72409	0.20838	0.46132
C42	0.77126	0.22979	0.49951
C43	0.79247	0.27688	0.53805
C44	0.76689	0.30178	0.53965
C45	0.30799	0.69177	0.83371
C46	0.35885	0.71795	0.83368
C47	0.07154	0.5351	0.83234
C48	0.04588	0.48557	0.8092
C49	0.99539	0.46029	0.80854
C50	0.96948	0.48383	0.83018
C51	0.99503	0.53334	0.85461
C52	0.04555	0.55865	0.85531
N53	0.91758	0.45586	0.82873
C54	0.52729	0.41535	0.82888
C55	0.6107	0.4224	0.82815
N56	0.62644	0.39049	0.82778
N57	0.58905	0.34618	0.8277
C58	0.54796	0.34803	0.82797
C59	0.56056	0.3963	0.82826
Cu60	0.59718	0.28974	0.82773
C61	0.38635	0.61415	0.83348
C62	0.3656	0.56702	0.79369
C63	0.39076	0.54171	0.79466
C64	0.43793	0.56312	0.83284
C65	0.45914	0.61021	0.87139
C66	0.43356	0.63511	0.87298
H67	0.28678	0.71176	0.16709
H68	0.06627	0.46573	0.12411
H69	0.9753	0.42006	0.12344
H70	0.9745	0.55295	0.20726
H71	0.06567	0.59877	0.20808

H72	0.48658	0.38946	0.16282
H73	0.63778	0.46284	0.16163
H74	0.51151	0.31315	0.16126
H75	0.32775	0.54906	0.09343
H76	0.37299	0.50326	0.09756
H77	0.49762	0.62851	0.23514
H78	0.45136	0.6729	0.24016
H79	0.62011	0.37843	0.5004
H80	0.3996	0.13239	0.45744
H81	0.3082	0.08671	0.45688
H82	0.30784	0.21961	0.5406
H83	0.399	0.26544	0.54142
H84	0.81991	0.05613	0.49617
H85	0.97112	0.12951	0.49496
H86	0.84485	-0.02018	0.49458
H87	0.66108	0.21572	0.42676
H88	0.70633	0.16992	0.43089
H89	0.83095	0.29518	0.56846
H90	0.78469	0.33957	0.57351
H91	0.28678	0.71176	0.83376
H92	0.06627	0.46572	0.79078
H93	0.9753	0.42006	0.7181
H94	0.9745	0.55295	0.87393
H95	0.06567	0.59877	0.87475
H96	0.48658	0.38946	0.82949
H97	0.63778	0.46284	0.82831
H98	0.51151	0.31315	0.82793
H99	0.32775	0.54906	0.7601
H100	0.37299	0.50326	0.76423
H101	0.49762	0.62851	0.1881
H102	0.45136	0.6729	0.90683

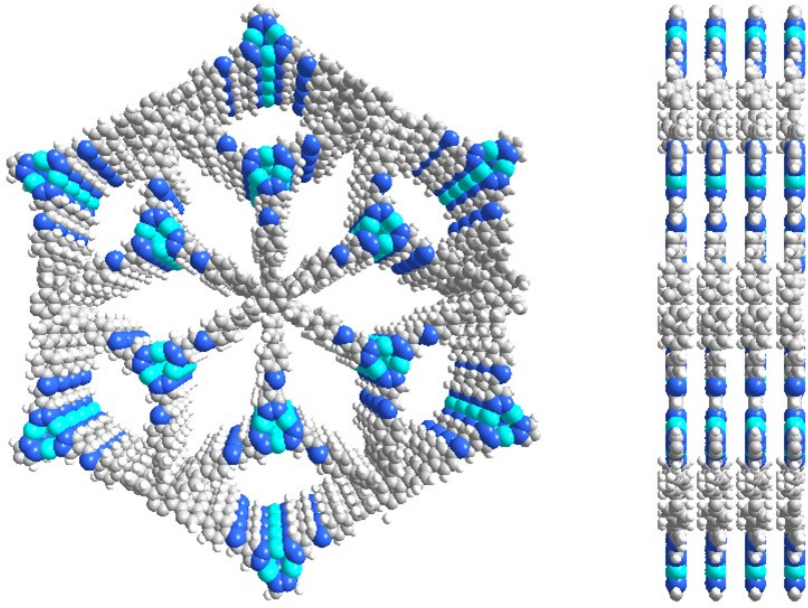


Fig. S23 Top (left) and side (right) views of **JNM-19** in AA stacking model.

Table S3. Atomic coordinates of the AA-stacking mode of **JNM-19**.

	X	Y	Z
C1	0.31793	0.53276	0.15471
N2	0.32001	0.57588	0.15302
N3	0.27571	0.56916	0.15222
C4	0.24358	0.52149	0.15296
C5	0.2695	0.49718	0.15456
C6	0.25018	0.44472	0.15698
N7	0.20376	0.41529	0.14669
C8	0.17984	0.36332	0.1504
C9	0.20247	0.33791	0.23526
C10	0.17736	0.28731	0.23746
C11	0.12918	0.2611	0.1565
C12	0.10656	0.28663	0.07467
C13	0.13166	0.33721	0.07303
C14	0.10256	0.20738	0.15826
C15	0.10762	0.18184	0.35279
C16	0.08222	0.13129	0.35461

C17	0.052	0.10526	0.16113
C18	0.04725	0.13064	-0.0338
C19	0.07188	0.18117	-0.03479
C20	0.02535	0.05131	0.1623
Cu21	0.62326	0.35958	0.15256
H22	0.34903	0.5277	0.15606
H23	0.20466	0.50584	0.15312
H24	0.27546	0.43149	0.16156
H25	0.23915	0.35666	0.30316
H26	0.19584	0.26867	0.30053
H27	0.06922	0.26751	0.01518
H28	0.11354	0.35622	0.01034
H29	0.13056	0.2009	0.50552
H30	0.08592	0.11231	0.50686
H31	0.02456	0.11114	-0.18516
H32	0.06757	0.19972	-0.18856

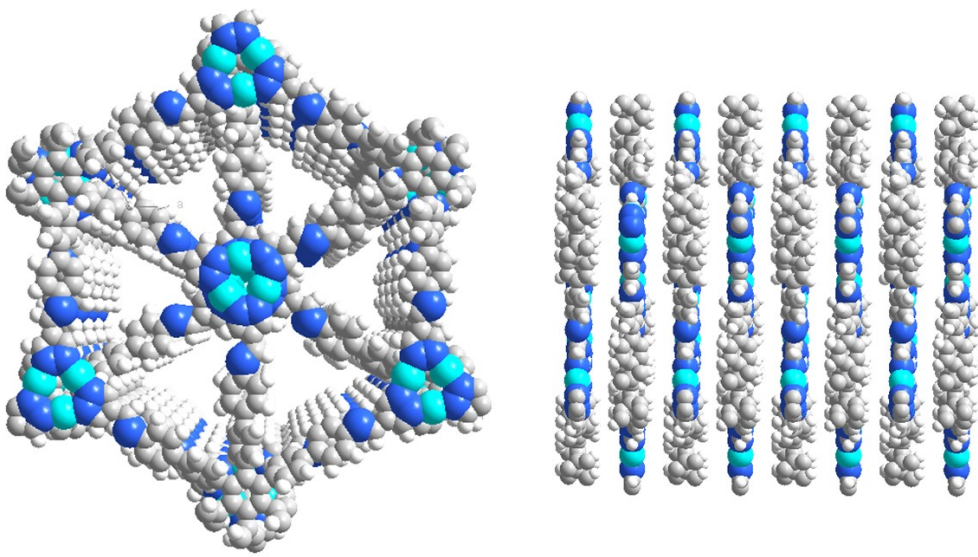


Fig. S24 Top (left) and side (right) views of **JNM-19** in AA stacking model.

Table S4. Atomic coordinates of the AB-stacking mode of **JNM-19**.

Space group: $P6_3$
 $a = b = 31.67 \text{ \AA}$, and $c = 12.52 \text{ \AA}$
 $\alpha = \beta = 90^\circ$, and $\gamma = 120$

	X	Y	Z
Cu1	0.59718	0.28974	0.16106
Cu2	0.93051	0.95641	0.4944
Cu3	0.59718	0.28974	0.82773
C4	0.30799	0.69177	0.16704
C5	0.52729	0.41535	0.16221
C6	0.6107	0.4224	0.16148
C7	0.54796	0.34803	0.1613
C8	0.56056	0.3963	0.16159
C9	0.38635	0.61415	0.16681
C10	0.3656	0.56702	0.12702
C11	0.39076	0.54171	0.12799
C12	0.35885	0.71795	0.16701
C13	0.43793	0.56312	0.16618
C14	0.45914	0.61021	0.20472
C15	0.43356	0.63511	0.20631
C16	0.64132	0.35844	0.50037
C17	0.69218	0.38462	0.50035
C18	0.40487	0.20177	0.4918
C19	0.37921	0.15224	0.47586
C20	0.32872	0.12696	0.4752
C21	0.30281	0.1505	0.49685
C22	0.32836	0.20001	0.52128

C23	0.07154	0.5351	0.16568
C24	0.37888	0.22532	0.52198
C25	0.86062	0.08202	0.49555
C26	0.94403	0.08907	0.49481
C27	0.88129	0.0147	0.49463
C28	0.89389	0.06297	0.49492
C29	0.71968	0.28082	0.50014
C30	0.04588	0.48557	0.14253
C31	0.69893	0.23369	0.46035
C32	0.72409	0.20838	0.46132
C33	0.77126	0.22979	0.49951
C34	0.79247	0.27688	0.53805
C35	0.76689	0.30178	0.53965
C36	0.30799	0.69177	0.83371
C37	0.35885	0.71795	0.83368
C38	0.07154	0.5351	0.83234
C39	0.04588	0.48557	0.8092
C40	0.99539	0.46029	0.80854
C41	0.99539	0.46029	0.14187
C42	0.96948	0.48383	0.83018
C43	0.99503	0.53334	0.85461
C44	0.04555	0.55865	0.85531
C45	0.52729	0.41535	0.82888
C46	0.6107	0.4224	0.82815
C47	0.54796	0.34803	0.82797
C48	0.56056	0.3963	0.82826
C49	0.96948	0.48383	0.16351
C50	0.38635	0.61415	0.83348
C51	0.3656	0.56702	0.79369
C52	0.39076	0.54171	0.79466
C53	0.43793	0.56312	0.83284
C54	0.45914	0.61021	0.87139
C55	0.43356	0.63511	0.87298
C56	0.99503	0.53334	0.18794
C57	0.04555	0.55865	0.18864
N58	0.62644	0.39049	0.16112
N59	0.58905	0.34618	0.16103
N60	0.25091	0.12253	0.4954
N61	0.95977	0.05716	0.49445
N62	0.92238	0.01285	0.49437
N63	0.91758	0.45586	0.82873
N64	0.62644	0.39049	0.82778
N65	0.58905	0.34618	0.8277
N66	0.91758	0.45586	0.16206
H67	0.37299	0.50326	0.76423
H68	0.49762	0.62851	0.1881
H69	0.45136	0.6729	0.90683
H70	0.28678	0.71176	0.16709
H71	0.06627	0.46573	0.12411
H72	0.9753	0.42006	0.12344

H73	0.9745	0.55295	0.20726
H74	0.06567	0.59877	0.20808
H75	0.48658	0.38946	0.16282
H76	0.63778	0.46284	0.16163
H77	0.51151	0.31315	0.16126
H78	0.32775	0.54906	0.09343
H79	0.37299	0.50326	0.09756
H80	0.49762	0.62851	0.23514
H81	0.45136	0.6729	0.24016
H82	0.62011	0.37843	0.5004
H83	0.3996	0.13239	0.45744
H84	0.3082	0.08671	0.45688
H85	0.30784	0.21961	0.5406
H86	0.399	0.26544	0.54142
H87	0.81991	0.05613	0.49617
H88	0.97112	0.12951	0.49496
H89	0.84485	-0.02018	0.49458
H90	0.66108	0.21572	0.42676
H91	0.70633	0.16992	0.43089
H92	0.83095	0.29518	0.56846
H93	0.78469	0.33957	0.57351
H94	0.28678	0.71176	0.83376
H95	0.06627	0.46572	0.79078
H96	0.9753	0.42006	0.7181
H97	0.9745	0.55295	0.87393
H98	0.06567	0.59877	0.87475
H99	0.48658	0.38946	0.82949
H100	0.63778	0.46284	0.82831
H101	0.51151	0.31315	0.82793
H102	0.32775	0.54906	0.7601

11. Photos for obtained samples



Fig. S25 Photo of $\mathbf{Cu}_3\mathbf{L}_3$.



Fig. S26 Photo of **JNM-18**.



Fig. S27 Photo of **JNM-19**.

12. Mott–Schottky plot

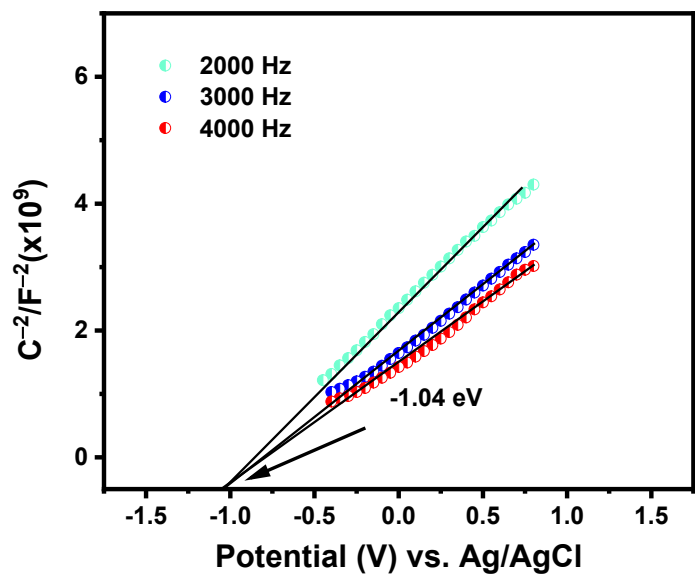


Fig. S28 Mott–Schottky of **JNM-18**.

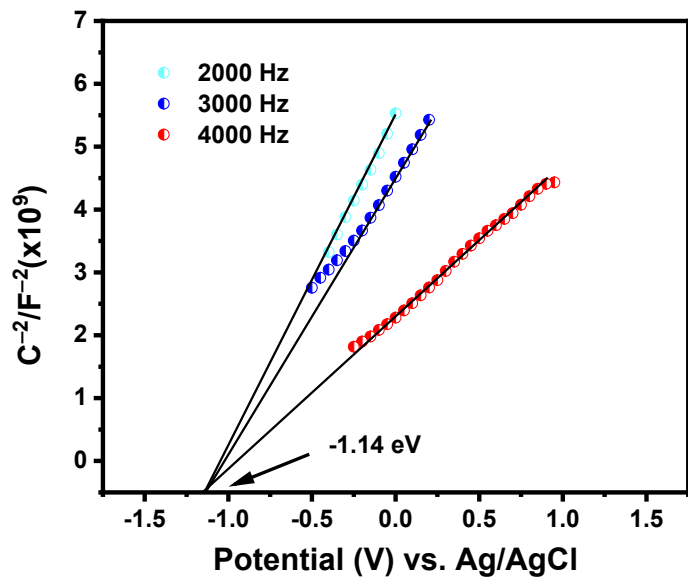


Fig. S29 Mott–Schottky of **JNM-19**.

13. Photocurrent response

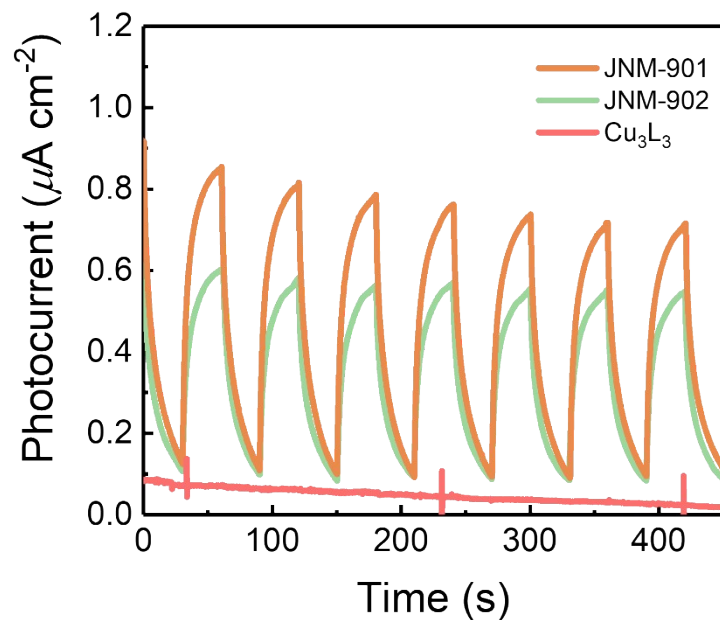


Fig. S30 Comparison of photocurrent responses of Cu_3L_3 , JNM-18 and JNM-19.

14. EPR experiment

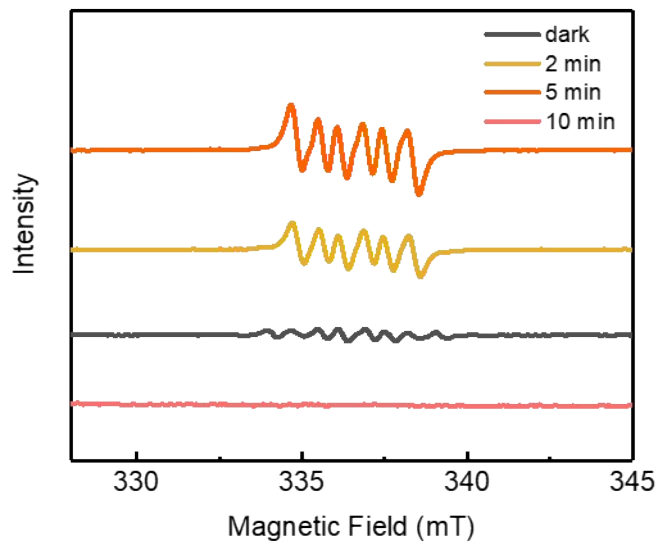


Fig. S31 EPR of JNM-19 under the dark and visible light illumination in the presence of DMPO.

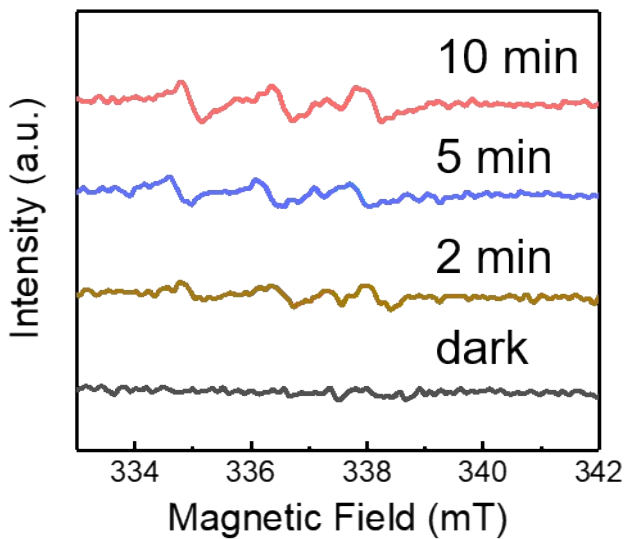


Fig. S32 EPR of JNM-18 under the dark and visible light illumination in the presence of TEMP.

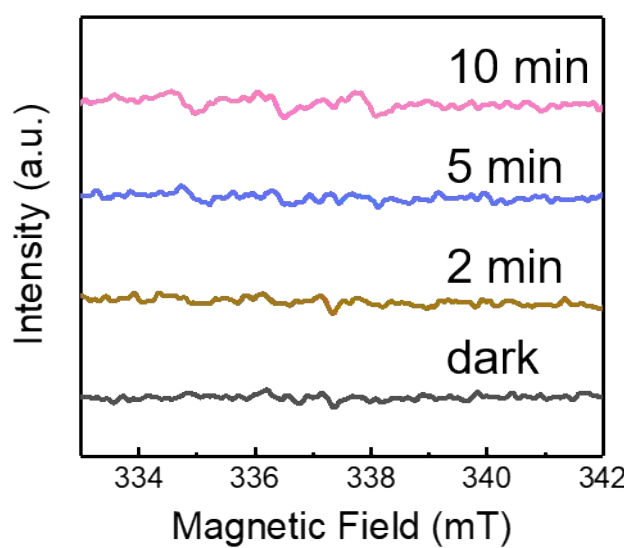


Fig. S33 EPR of **JNM-19** under the dark and visible light illumination in the presence of TEMP.

15. Evaluation of the $\text{O}_2^{\bullet-}$ generation efficiency

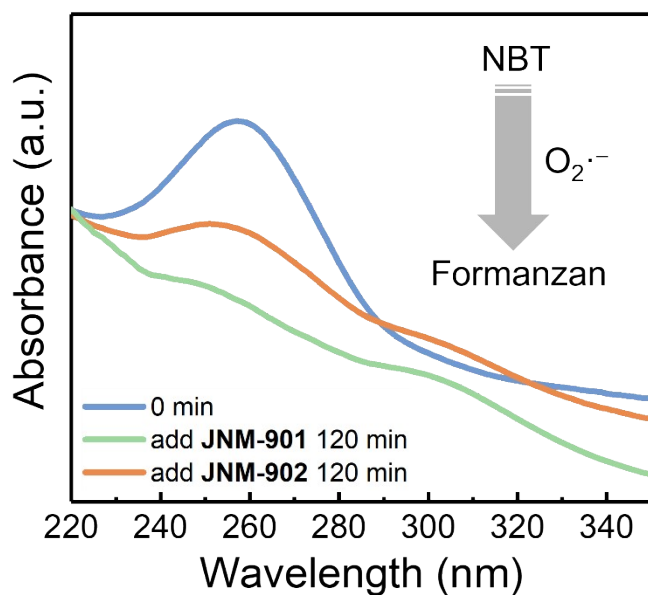


Fig. S34 UV–vis absorption spectra of NBT with the addition of **JNM-18** and **JNM-19** upon visible light irradiation.

16. Photocatalytic Application

16.1 General procedure



A solution of benzylamine (0.3 mmol) and photocatalyst (3% based on Cu_x) in CH_3CN (2 mL) was stirred under 12 W violet LED (395 nm) for 12 h at room temperature. The yields were determined by ¹H NMR spectrum by calculating the integration of singlet peak of methylene proton in the products (at about 4.84 ppm for $-\text{CH}=\text{N}-\text{CH}_2-$) and that of the corresponding proton in the starting materials (at about 3.90 ppm as singlet for $\text{H}_2\text{N}-\text{CH}_2-$). Controlled experiments were investigated in a similar procedure. No Au ion was found in the supernatant suggested by ICP measurement.

16.2 Recyclability

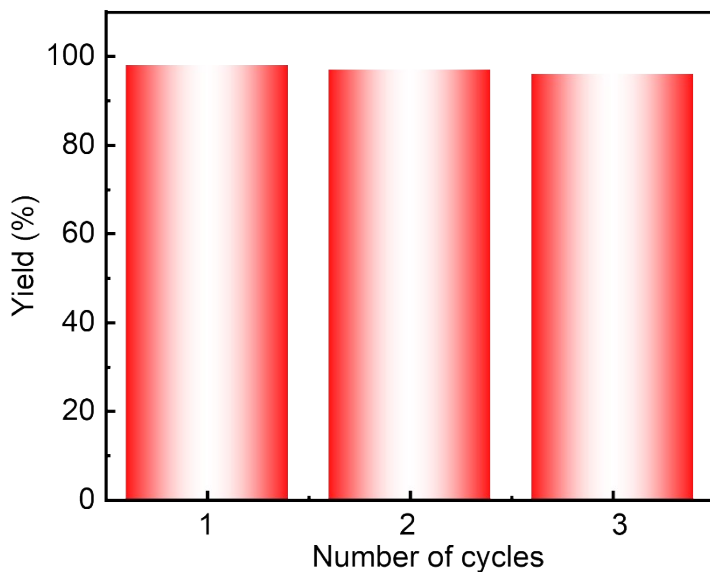


Fig. S35 Recyclability of JNM-18 as the photocatalyst for benzylamine oxidations.

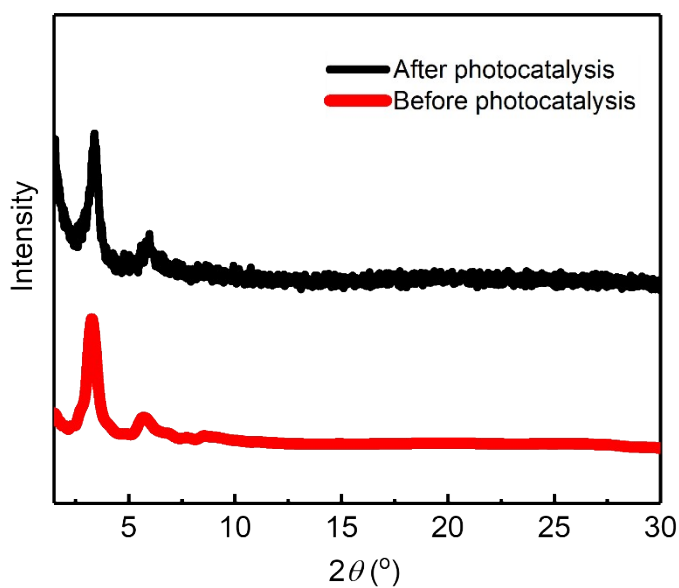


Fig. S36 Comparison of PXRD patterns of the As-synthesized **JNM-18** catalysts and that after photocatalyzed reaction of benzylamine oxidations.

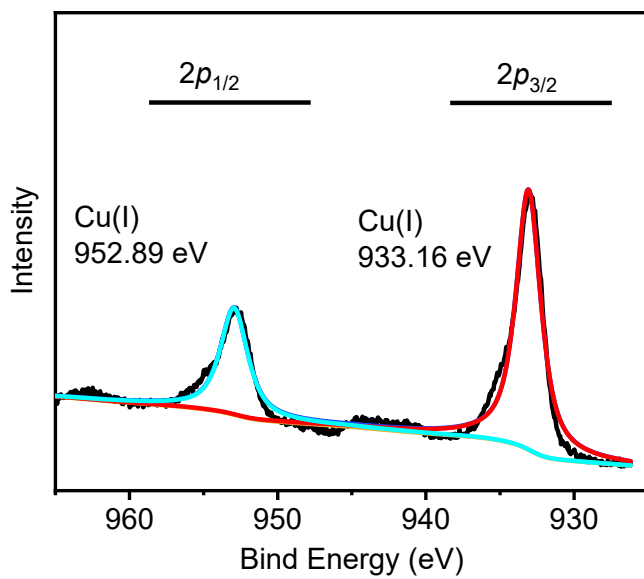


Fig. S37 XPS for **JNM-18** after photocatalyzed reaction of benzylamine oxidations.

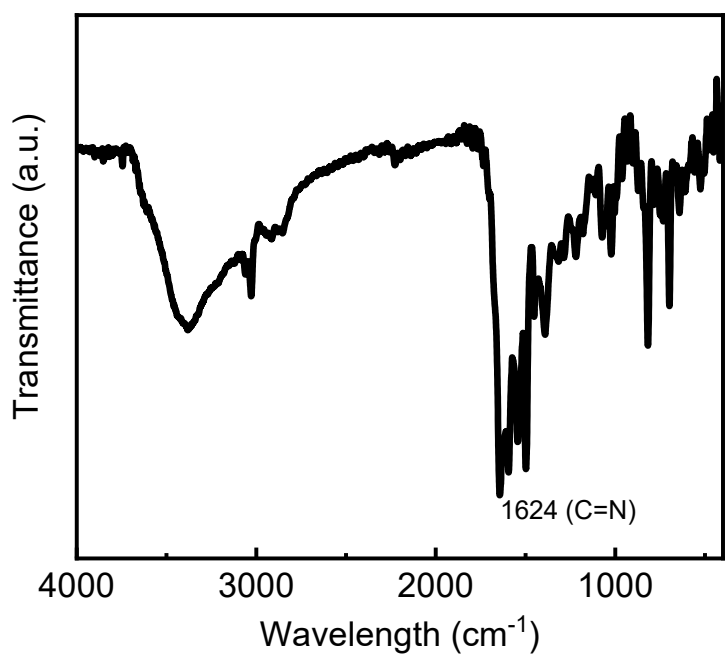


Fig. S38 FT-IR spectra of **JNM-18** after photocatalyzed reaction of benzylamine oxidations.

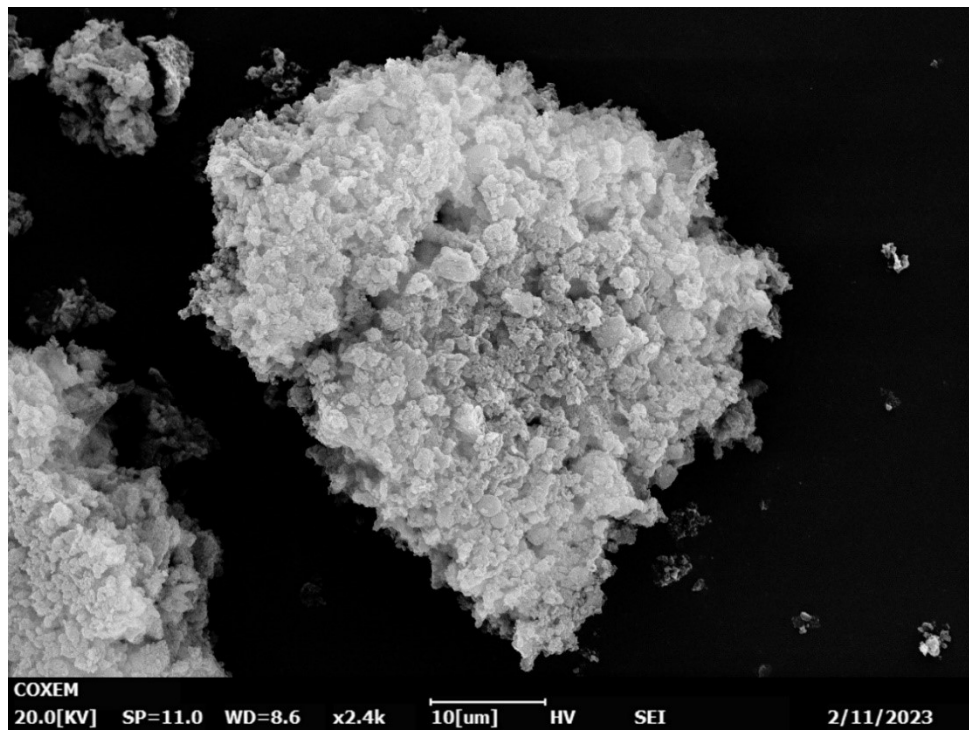


Fig. S39 SEM of **JNM-18** after photocatalyzed reaction of benzylamine oxidations.

16.3 Aerobic oxidation of secondary amines

Table S5. Photocatalyzed aerobic oxidation of secondary amines to imines by **JNM-18**.^a

Entry	Substrate	Product	Yield (%)
1			75
2			40
3			78
4			47
5			62

^aReaction condition: amine (0.3 mmol), **JNM-18** (3 mol %), CH₃CN (2 mL), rt, violet LED (12 W), air. The reported yields presented are based on ¹H NMR spectra.

16.4 Mechanism

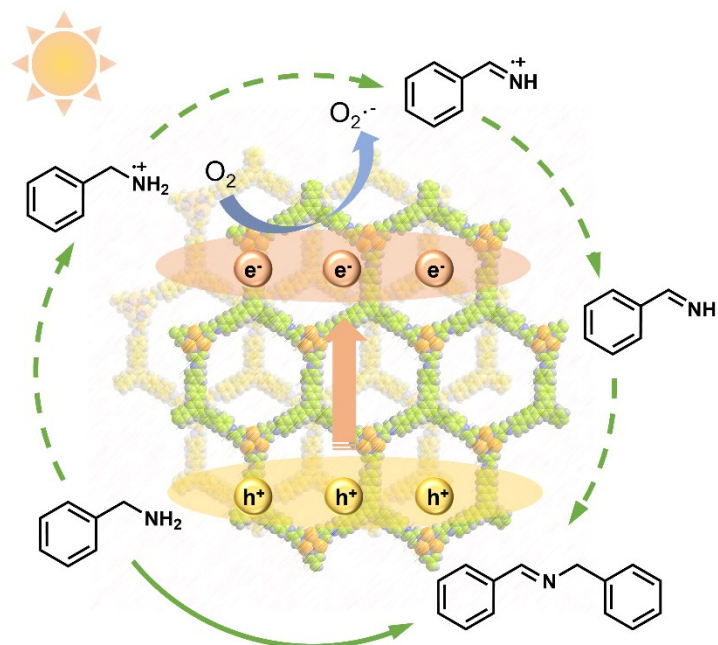
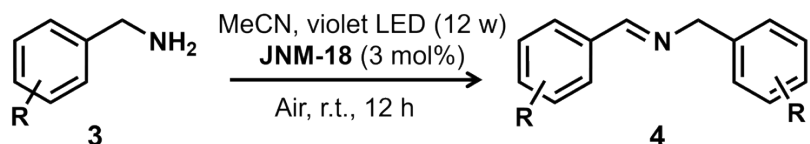
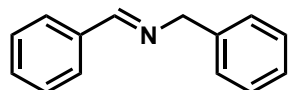


Fig. S40 Proposed reaction mechanism of the photocatalyzed aerobic oxidation of benzylamine by **JNM-18**.

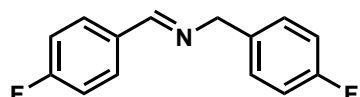
16.4 Scope of JNM-18 Catalyst for oxidations of amines.



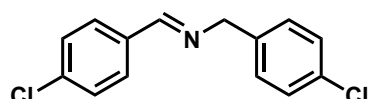
A solution of amine (1.0 equiv, 0.3 mmol) and **JNM-18** (3% based on Cu,) in CH₃CN (2 mL) was stirred under 12 W violet LED for 12 h at room temperature. The yields were determined by ¹H NMR spectrum by calculating the integration of singlet peak of methylene proton in the products (at about 4.84 ppm for -CH=N-CH₂-) and that of the corresponding proton in the starting materials (at about 3.90 ppm as singlet for H₂N-CH₂-).



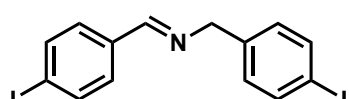
4a. ¹H NMR (400 MHz, 298 K, CDCl₃) δ 8.44 (s, 1H), 7.82 (s, 2H), 7.43 (d, *J* = 32.4 Hz, 8H), 4.87 (s, 2H).



4b. ¹H NMR (400 MHz, 298 K, CDCl₃) δ 8.35 (s, 1H), 7.77 (dd, *J* = 8.6, 5.7 Hz, 2H), 7.30 (dd, *J* = 8.5, 5.5 Hz, 2H), 7.10 (t, *J* = 8.6 Hz, 2H), 7.04 (t, *J* = 8.7 Hz, 2H), 4.76 (s, 2H).

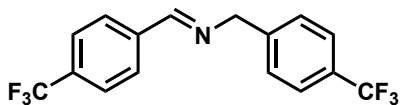


4c. ¹H NMR (400 MHz, 298 K, CDCl₃) δ 8.40 (s, 1H), 7.41 (d, *J* = 8.3 Hz, 2H), 7.35 (s, 2H), 7.26 (t, *J* = 6.1 Hz, 4H), 4.79 (s, 2H).

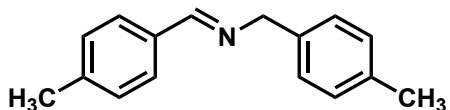


4d. ¹H NMR (400 MHz, 298 K, CDCl₃) δ 8.32 (d, *J* = 1.5 Hz, 1H), 7.79 (s, 2H), 7.69

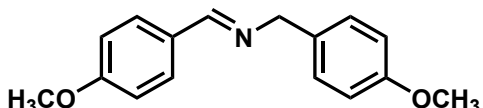
(d, $J = 8.3$ Hz, 2H), 7.51 (d, $J = 8.4$ Hz, 2H), 7.10 (d, $J = 8.3$ Hz, 2H), 4.75 (s, 2H).



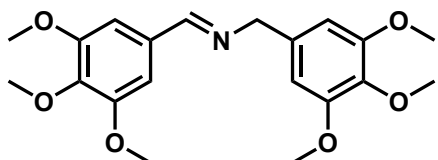
4e. ^1H NMR (400 MHz, 298 K, CDCl_3) δ 8.47 (s, 1H), 7.91 (d, $J = 8.0$ Hz, 2H), 7.69 (d, $J = 8.0$ Hz, 2H), 7.62 (d, $J = 8.0$ Hz, 2H), 7.48 (d, $J = 8.0$ Hz, 2H), 4.90 (s, 2H).



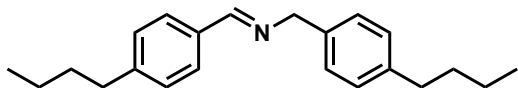
4f. ^1H NMR (400 MHz, 298 K, CDCl_3) δ 8.38 (s, 1H), 7.71 (d, $J = 8.0$ Hz, 2H), 7.20 (d, $J = 5.5$ Hz, 6H), 4.80 (s, 2H), 2.41 (s, 3H), 2.38 (s, 3H).



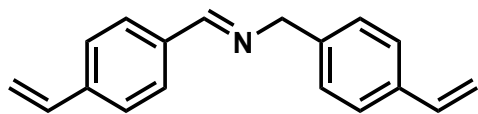
4g. ^1H NMR (400 MHz, 298 K, CDCl_3) δ 8.40 (s, 1H), 7.74 (d, $J = 8.7$ Hz, 2H), 7.27 (d, $J = 8.5$ Hz, 2H), 6.95 (d, $J = 6.7$ Hz, 2H), 6.90 (s, 2H), 4.75 (s, 2H), 3.85 (s, 3H), 3.82 (s, 3H).



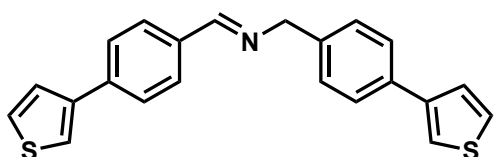
4h. ^1H NMR (400 MHz, 298 K, CDCl_3) δ 8.23 (s, 1H), 6.99 (s, 2H), 6.49 (s, 2H), 4.68 (s, 2H), 3.85 – 3.77 (m, 18H).



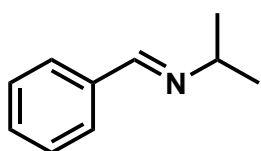
4i. ^1H NMR (400 MHz, 298 K, CDCl_3) δ 8.39 (s, 1H), 7.74 (d, $J = 7.9$ Hz, 2H), 7.28 (d, $J = 4.0$ Hz, 4H), 7.21 (s, 2H), 4.82 (s, 2H), 2.69 – 2.64 (m, 4H), 1.66 – 1.61 (m, 4H), 1.43 – 1.37 (m, 4H), 0.98 (dd, $J = 7.3, 2.9$ Hz, 6H).



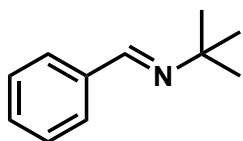
4j. ^1H NMR (400 MHz, 298 K, CDCl_3) δ 8.32 (s, 1H), 7.77 (d, $J = 8.0$ Hz, 2H), 7.54 – 7.31 (m, 6H), 6.89 – 6.64 (m, 2H), 5.81 (dd, $J = 34.5, 17.6$ Hz, 2H), 5.30 (dd, $J = 38.4, 10.8$ Hz, 2H), 4.84 (d, $J = 7.5$ Hz, 2H).



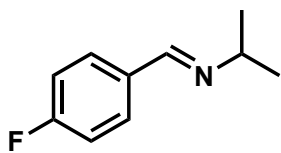
4k. ^1H NMR (400 MHz, 298 K, CDCl_3) δ 8.43 (s, 1H), 7.52 – 7.18 (m, 6H), 7.16 – 6.88 (m, 8H), 4.96 (s, 2H).



6a. ^1H NMR (400 MHz, 298 K, CDCl_3) δ 8.25 (s, 1H), 7.71 – 7.65 (m, 2H), 7.43 – 7.36 (m, 2H), 7.38 – 7.31 (m, 1H), 3.61 (dq, $J = 15.0, 7.5$ Hz, 1H), 1.21 (d, $J = 7.5$ Hz, 6H).



6b. ^1H NMR (400 MHz, 298 K, CDCl_3) δ 8.11 (s, 1H), 7.73 – 7.67 (m, 2H), 7.43 – 7.36 (m, 2H), 7.39 – 7.31 (m, 1H), 1.26 (s, 7H).



6c. ^1H NMR (400 MHz, 298 K, CDCl_3) δ 8.26 (s, 1H), 7.69 – 7.63 (m, 2H), 7.14 – 7.07 (m, 2H), 3.62 (p, $J = 7.5$ Hz, 1H), 1.21 (d, $J = 7.5$ Hz, 6H).

17. Computational Details

Density functional theory (DFT) was performed for **JNM-18** and **JNM-19** by using Gaussian 09 software.¹ The following level of theory was adopted in all the calculations: (1) Functional: the hybrid B3LYP in conjunction with D3(BJ) dispersion correlation;^{2,3} (2) Basis sets: the LANL2DZ⁴⁻⁷ effective core potential (ECP) was used for Cu and the 6-31G(d,p)⁸ basis set was used for the other atoms. Firstly, the geometrical optimization was performed for the monomers of all the above compounds to obtain their stable ground-state (S_0) geometries by restricted B3LYP method, confirmed by the absent of imaginary frequencies (NIMG = 0). The Electrostatic potential (ESP) surface maps were obtained in Gaussian view based on the optimized structures.

18. Reference

- 1 M. J. Frisch, G. W. Trucks, H. B. Schlegel, G. E. Scuseria, M. A. Robb, J. R. Cheeseman, G. Scalmani, V. Barone, B. Mennucci, G. A. Petersson, H. Nakatsuji, M. Caricato, X. Li, H. P. Hratchian, A. F. Izmaylov, J. Bloino, G. Zheng, J. L. Sonnenberg, M. Hada, M. Ehara, K. Toyota, R. Fukuda, J. Hasegawa, M. Ishida, T. Nakajima, Y. Honda, O. Kitao, H. Nakai, T. Vreven, Jr. J. A. Montgomery, J. E. Peralta, F. Ogliaro, M. Bearpark, J. J. Heyd, E. Brothers, K. N. Kudin, V. N. Staroverov, R. Kobayashi, J. Normand, K. Raghavachari, A. Rendell, J. C. Burant, S. S. Iyengar, J. Tomasi, M. Cossi, N. Rega, J. M. Millam, M. Klene, J. E. Knox, J.B. Cross, V. Bakken, C. Adamo, J. Jaramillo, R. Gomperts, R. E. Stratmann, O. Yazyev, A. J. Austin, R. Cammi, C. Pomelli, J. Ochterski, R. L. Martin, K. Morokuma, V. G. Zakrzewski, G. A. Voth, P. Salvador, J. J. Dannenberg, S. Dapprich, A. D. Daniels, O. Farkas, J. B. Foresman, J. V. Ortiz, J. Cioslowski and D. J. Fox, Gaussian 09 (Revision E.01), Gaussian, Inc., Wallingford, CT, 2013.
- 2 S. Grimme, J. Antony, S. Ehrlich and H. Krieg, A consistent and accurate ab initio parametrization of density functional dispersion correction (DFT-D) for the 94 elements H-Pu, *J. Chem. Phys.*, 2010, **132**, 154104.
- 3 S. Grimme, S. Ehrlich and L. Goerigk, Effect of the damping function in dispersion corrected density functional theory, *J. Comput. Chem.*, 2011, **32**, 1456–1465.
- 4 T. H. Dunning, Jr., and P. J. Hay, In Modern Theoretical Chemistry; Schaefer, H. F., III., Ed.; Plenum: New York, 1976, Vol. 3, pp 1–28.
- 5 P. J. Hay and W. R.Wadt, *Ab initio* effective core potentials for molecular calculations. Potentials for the transition metal atoms Sc to Hg, *J. Chem. Phys.*, 1985, **82**, 270.
- 6 W. R.Wadt and P. J. Hay, *Ab initio* effective core potentials for molecular calculations. Potentials for main group elements Na to Bi, *J. Chem. Phys.*, 1985, **82**, 284.
- 7 P. J. Hay and W. R.Wadt, *Ab initio* effective core potentials for molecular calculations. Potentials for K to Au including the outermost core orbitals, *J. Chem.*

Phys., 1985, **82**, 299.

- 8 P. C. Hariharan, and J. A. Pople, A. Accuracy of AH n equilibrium Geometries by Single Determinant Molecular Orbital Theory, *Mol. Phys.*, 1974, **27**, 209.